

Dual-Resonator Kinetic-Inductance Detector for Distinction between Signal and 1/f Frequency Noise

N. Foroozani,^{1,2,*} B. Sarabi,¹ S. H. Moseley,³ T. Stevenson,³ E. J. Wollack,³ O. Noroozian,³ and K. D. Osborn^{1,4,*}

¹*Laboratory for Physical Sciences, University of Maryland, College Park, MD 20740, USA*

²*Department of Physics, University of Maryland, College Park, MD 20742, USA*

³*NASA Goddard Space Flight Center, Greenbelt, MD 20771, USA*

⁴*Joint Quantum Institute, University of Maryland, College Park, MD 20742, USA*

(Dated: February 24, 2022)

Astronomical Kinetic Inductance Detectors (KIDs), similar to quantum information devices, experience performance limiting noise from materials. In particular, 1/f (frequency) noise can be a dominant noise mechanism, which arises from Two-Level System defects (TLSs) in the circuit dielectrics and material interfaces. Here we present a Dual-Resonator KID (DuRKID), which is designed for improved signal to noise (or noise equivalent power) relative to 1/f-noise limited KIDs. We first show the DuRKID schematic, fabricated circuit, and we follow with a description of the intended operation, first measurements, theory, and discussion. The circuit consists of two superconducting resonators sharing an electrical capacitance bridge of 4 capacitors, each of which hosts TLSs. The device is intended to operate using hybridization of the modes, which causes TLSs to either couple to one mode or the other, depending upon which capacitor they reside in. In contrast, the intended KID signal is directed to an inductor, and due to hybridization this causes correlated frequency changes in both (hybridized) modes. Therefore, one can distinguish photon signal from TLS frequency noise. To achieve hybridization, a TiN inductor is current biased to allow tuning of one bare resonator mode into degeneracy with the other and measurements show that the intended resonator modes frequency tune and hybridize as expected. The interresonator coupling and unintentional coupling of the 2 resonators to transmission lines are also characterized in measurements. In the theory, based on a quantum-information-science modes, we calculate the 4-port S parameters and simulate the 1/f frequency noise of the device. The study reveals that the DuRKID can exhibit a large and fundamental performance advantage over 1/f-noise-limited KID detectors.

I. INTRODUCTION

Kinetic Inductance Detectors (KIDs) [1–4] for astronomy contain resonators which experience noise, related to noise in qubits for quantum information processing (QIP) [5–9]. For KID-based millimeter and submillimeter-wave astronomical imaging systems [10–12] the signal band of interest has frequency noise which appears as a strong 1/f-like noise spectrum. This necessitates implementing scan strategies and signal modulation techniques to mitigate their influence on the final observational data products in order to achieve the underlying device sensitivity [13–15]. More generally speaking, if unaddressed in such applications – the presence of residual low frequency variations introduces correlated noise which can lead to increased effective noise levels and systematic artifacts that include image striping and amplitude calibration errors. While significant progress has been made over the past two decades in reducing low frequency noise in KIDs, developing sensitive detectors with lower noise remains the primary technical challenge for many current and future astrophysical observatories [16–18].

A major limitation to the performance in KIDs and qubits arises from the same defect type, that is a two-level system (TLS) defect residing in a dielectric or at a material interface within the device. KIDs are perturbed in resonance frequency by the photon signal, however, TLSs meanwhile induce 1/f frequency noise which causes

difficulties in signal detection. Similarly, in QIP the qubit transition frequency experiences frequency noise from TLSs [5, 19]. This noise necessitates recalibration of pulse-driven qubit logic gates [20, 21]. Recent studies of TLS noise mechanisms for KIDs and qubits have shown the importance of a more in-depth understanding of TLSs [5, 19, 21–23]. Two recent theories explain that the interaction between TLSs is responsible for 1/f frequency noise whereby low-frequency thermally fluctuating TLSs influence high-frequency (near-resonance) TLSs [24, 25], which in turn interacts with the high frequency superconducting mode [26, 27]. Traditionally there is a strategy to minimize the influence of TLSs in KIDs and qubits through material choices [28–32] and geometry optimization [4]. While increasing the measurement power lowers the frequency noise from TLSs, it also generates quasiparticles. This leads to obfuscation of the KID photon signal, because the signal is also produced by generating quasiparticles [33].

Recognizing that practical limitations to frequency noise in KIDs remain, we propose to tackle the problem differently. Here we describe a detector circuit that can allow one to distinguish photon signal from TLS frequency noise. The circuit uses two resonators coupled with an electrical capacitance bridge. It is a type of KID as the design allows a shift of an inductor value caused by a photon signal, similar to a standard KID. Here the inductance shift causes (correlated) frequency

shifts of both resonators. However, in the proposed KID configuration the TLSs can only cause uncorrelated frequency shifts in the resonator modes, because it merely assumes that high-frequency TLS noise from different capacitors will be independent. We use established circuit quantum electrodynamics (cQED) analysis to model the circuit, which includes TLSs as a noise source. In the next section we present the circuit schematic for the device, named a Dual-Resonator KID (DuRKID), which has electrical-bridge coupling of resonators. Fabrication, details of the DuRKID and the data from the device, including frequency tuning and hybridization are shown in this section. In section III, an analysis of the DuRKID is described with representative TLSs. The analysis is used to extract the dielectric's loss from resonator data, and with a new method, extract unintended resonator-to-transmission line coupling. We conclude in section IV.

II. DEVICE DESIGN, METHOD OF NOISE DISTINCTION AND FREQUENCY TUNING MEASUREMENT

TLSs shift the resonator frequency, as does the photon signal, in standard KIDs. The former effectively causes a time change in the frequency dependent dielectric constant, and the latter causes an increase in a superconductor's kinetic inductance [34]. We propose the DuRKID, a device with two resonator modes in contrast to standard KIDs, to improve the noise sensitivity that is hampered by TLS-induced frequency shifts. In the DuRKID, we find that noise from TLSs should be qualitatively different from the signal such that the two are distinguishable and the effective signal sensitivity is improved.

We begin with a discussion of a standard-coupled resonator pair, where LC resonators are nominally the same frequency (degenerate) prior to coupling. This reference case is shown in Fig. 1(a), where the resonators are inductively coupled through M (although they could instead be coupled through a capacitor for the same effect). In the schematic, each bare (uncoupled) resonance mode frequency, $f_{r,A}$ and $f_{r,B}$, is created by an individual inductor, L_A and L_B , respectively. Without resonator coupling, a given TLS in the capacitor of each resonator will couple solely to the field of that resonator, and the resonators would act as two separate KIDs. For each mode, one TLS causes a dispersion (frequency shift): $\Delta f_r = g^2/(f_{TLS} - f_{res})$, where f_{TLS} is the TLS frequency. In contrast, if the resonators are set to the same bare frequency, coupling will hybridize them and a typical TLS (which is weakly coupled) on either capacitor will interact with both modes through the same coupling term g , and hence cause correlated noise in the modes. One case that is especially troublesome is for TLSs between the mode frequencies, since their motion may cause a correlated but quantitatively different drift

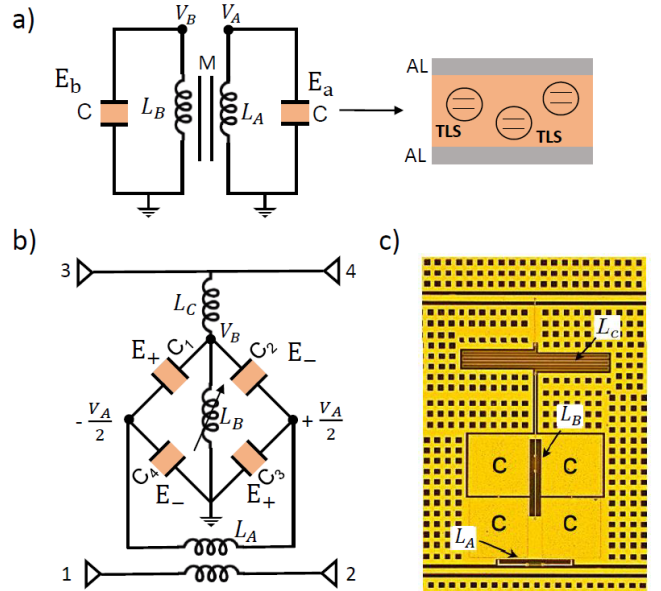


FIG. 1. (a, b) Resonators with two modes (an extra mode relative to a standard MKID). If the modes are far detuned (in frequency), the modes are effectively decoupled from each other and also experience different TLS noise environments. (a) Standard-coupled resonator circuit. When the two modes are hybridized, TLS noise from both capacitors will equally influence the two resonator modes: $E_a(t) = E_b(t)$ and $E_a(t) = -E_b(t)$. (b) Circuit schematic of Dual-Resonator KID (DuRKID). An electrical bridge of nominally equal capacitances ($C_1 - C_4$) creates capacitance for the modes. Spatial resonator modes A and B, with voltage components V_A and V_B , are hybridized for equal L_A and L_B by their stray coupling. For the hybridized mode where $V_A(t)$ and $V_B(t)$ are in-phase, the electric field in capacitors 1 and 3 adds $E_+ \propto \langle a + b \rangle$, but in 2 and 4 the electric fields are out-of-phase and cancel $E_- \propto \langle a - b \rangle$. For the other hybridized mode, the location of constructive and destructive interference is swapped. This gives selective sensitivity to the TLS noise sources according to the capacitor which hosts it. In this schematic a dc current applied to port 3 may tune inductance L_B . (c) Optical image of the fabricated DuRKID with the same (opposite) orientation as Device 1 and 3 (2) in Fig. 3(a). The materials include: Si substrate (black), aluminum (yellow), TiN (dark red), and silicon nitride dielectric (obscured).

in both modes (from the TLS frequency drift and dispersion). However, a signal fed to one of the inductors will also cause a correlated change in the frequencies. Thus, in a standard-coupled resonator pair, hybridized modes will exhibit correlated TLS noise that provides no obvious method of distinction from signal.

In this work we propose to use an alternative two-resonator device that we designate a DuRKID. To differentiate the TLS noise from signal, the device uses an electrical bridge for coupling between the modes (see Fig. 1(b)), which breaks the degeneracy between the signals of interest and the TLS induced fluctuation noise. As

in the standard-coupled resonator circuit, we have bare (uncoupled) resonance mode A and B comprised of an individual inductor, L_A and L_B , respectively, but the bridge provides a shared set of four capacitors. The capacitors are nominally equal such that both modes access the same nominal capacitance. The coupling according to the figure shows that mode $A(B)$ is intentionally coupled to the transmission line with ports 1 and 2 (3 and 4). However, when hybridized, each mode is coupled to both transmission lines. To create degeneracy between these bare modes, L_B is designed to be current biased. For example, by using port 3 we can decrease the higher mode frequency of device 2 (see Figs. 1(c) and 2(a)). For the sake of pedagogy, in this work we consider this inductor as analogous to the KID readout inductor because it can be changed in frequency, similar to the way a KID has an inductor that is changed in frequency by the signal.

As mentioned above, the bridge-coupled resonator pair acts differently than a standard-coupled resonator pair. A TLS in a bridge of the capacitor is equally shared by both modes before hybridization. However, once hybridized, one field mode amplitude is zero in 2 of the 4 capacitors. Likewise, it becomes zero in the other 2 capacitors for the other hybridized mode. *Thus, a given TLS will only frequency-shift (disperse) one of the hybridized modes in a bridge coupled resonator. In contrast, a change in the frequency from incident photons will cause a correlated shift to both modes such that it can be distinguished from TLS noise.*

A fabricated DuRKID is shown in Fig. 1(c). Many DuRKIDs are fabricated together on a high-resistivity (>20 k Ω .cm) silicon wafer. The base superconducting layer is a TiN-Al bi-layer, with 15 nm thick TiN and a 250 nm thick Al. This bilayer was patterned followed by the removal of Al to leave TiN bare in certain locations to provide kinetic inductances L_{kA} , L_{kB} and L_{kC} as part of the total inductances L_A , L_B and L_C , respectively. The dielectric layer for the capacitor bridge is a high-density silicon nitride (SiNx) film with a nominal thickness of 275 nm deposited using PECVD. [35]. Then via holes are made using SF₆ reactive ion etching. A 250 nm sputtered Al film forms the counter electrode of the capacitor bridge. After patterning the counter electrode, excess SiN_x is removed from most of the sample area to allow access to the leads on the base layer. Three devices are fabricated per chip, as shown in the device layout of Fig. 2(a). Devices 1 and 3 are not rotated relative to Fig. 1(b-c) such that they share galvanic coupling to port 1. Device 2, the center device, is the only device that is galvanically coupled to port 3, due to a π rotation of the device relative to Fig. 1(c).

The devices are cooled down to 20 mK in a dilution refrigerator. The transmission data $|S_{21}|$ and $|S_{43}|$ for all three devices are shown in Fig. 2(b) when $I_b = 0$. The devices were intentionally designed with differing offsets between the two resonator modes at zero bias current, I_b .

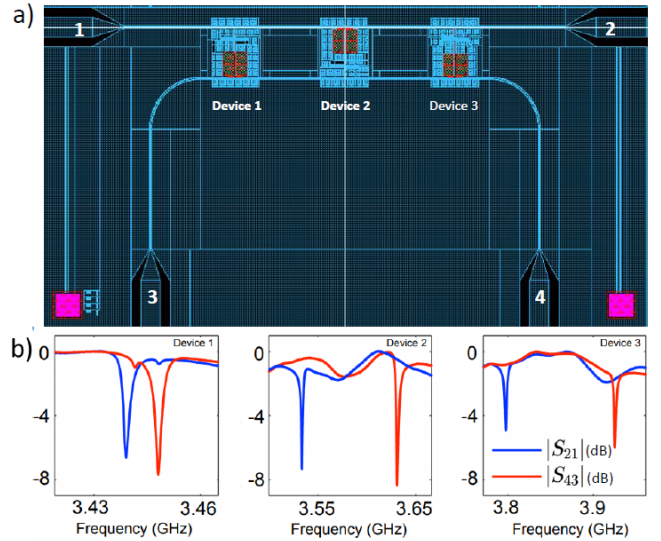


FIG. 2. (a) Device layout of three devices on a chip with two feedlines for each device. One resonator of each device is tunable, using the nonlinear inductance L_B . The LC resonances are mainly defined by a 0.6 nH inductor and trilayer capacitors with $C=3.14$ pF, containing a 275 nm thick silicon nitride dielectric film. (b) Measured transmission $|S_{21}|$ and $|S_{43}|$ for devices 1, 2, and 3 at $I_b = 0$.

The offset (detuning) between two modes for each dual resonator is measured at $\delta_1 = 9$ MHz, $\delta_2 = 97$ MHz and $\delta_3 = 128$ MHz, respectively. As planned, the tunable resonance at zero bias was at a higher frequency than the non-tunable resonance in all three devices. All devices tune with bias current to reach degeneracy. For device 3 the tuning for degeneracy is large ~ 128 MHz which is enabled by large kinetic inductance change from the unbiased inductance per square of 56 pH. The fractional frequency tuning $\delta f_r/f_r = 3.5\%$ is approximately an order of magnitude higher than achieved with a magnetic-field tuned CPW resonator [36].

Data on device 2 transmission $|S_{43}|(f, I_b)$ is shown in Fig. 3(a) and (b), which shows frequency tuning of the resonance versus bias current. This device has an independent bias line and thus a precisely known bias current. The applied bias current shifts the higher mode toward the lower resonance and the tunable resonator disappears at a bias $I_{b,max} = 210\mu A$, indicating a change to the normal state, likely at the wiring vias. Although most of the geometric inductor length within each resonator is provided by Al, the kinetic inductance L_{kA} and L_{kB} make for approximately 85% of the total inductance L_A and L_B . At temperatures much smaller than the superconducting critical temperature T_c , the nonlinear response of L_k to I_b can be expanded as $L_k(I_b) = L_k(0)(1 + (\frac{I_b}{I'})^2 + \dots)$, where I' sets the scale of nonlinearity. By considering up to quadratic order in $L_k(I_b)$, we extract from a fit to L_{kB} that $I' = 789\mu A$ (See Fig. 6 in Appendix A).

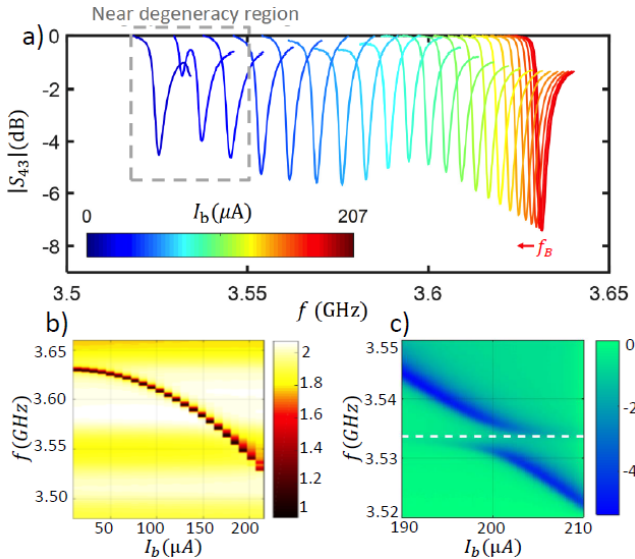


FIG. 3. Data on device 2. Transmission spectra, $|S_{43}|$, of tunable resonator with applied bias current up to 210 μ A, measured at 20 mK. (a) Each color represents one $|S_{43}(f)|$ trace at a separate DC bias. The frequency of the resonator B, as shown by the S_{43} , shifts down from 3.635 GHz to 3.52 GHz, by 120 MHz, when the minimum bias is applied for full hybridization. (b) $S_{43}(f, I_b)$ plot that emphasizes resonance frequency versus bias over the entire applied current range I_b . (c) Measured transmission $|S_{43}|$ of device B versus frequency f_B and tuning current I_b near degeneracy shows avoided crossing due to hybridization with the fixed mode at $f_A=3.533$ GHz. From the analysis, a coupling of $\Omega_{AB}/2\pi = 5.1$ MHz was obtained.

$|S_{43}|$ at different I_b (Fig. 3(c)) shows an avoided crossing due to hybridization with the A mode. We also measured the cross coupling from the input port of one transmission line to the output port of the other, S_{41} and S_{23} . The transmission $|S_{41}|$ for hybridization degenerate modes is on the order of -10dB (not shown), indicating some internal loss in the resonators but also sufficiently high coupling of the resonators to their intended transmission lines. The capacitors of the bridge were carefully designed in layout to be equal. As a result, the mutual inductance is likely the dominant coupling mechanism. We note that the splitting from mode coupling must be larger than other line widths for the device to operate as intended. To further analyze the data quantitatively, we applied the two-resonator model, to fit the transmission data, S_{21} and S_{43} with the fitting procedure explained in the Appendix. From Fig. 3(c) we obtained the inter-resonator coupling of $\Omega_{AB}/2\pi = 5.1$ MHz. This coupling agreed with simulation, within a factor of 2. We then use this as a fixed parameter in the device model for two separate fitting procedures. In the first fit procedure we fit both standard transmission data at the same time, according to a procedure as described in the Appendix B. From this we extract the internal Q-factor of 2750 and 3100 for resonators A

and B respectively. Viewed as a material loss tangent $\tan\delta = 1/Q_i = (3.4 \pm 0.2) \times 10^{-4}$, the values match our expectations for recipe of the PECVD SiN_x used. It has a lower loss than typical AlO_x by approximately an order of magnitude [37]. In other work, silicon-on-insulator (SOI) is used for higher Q-factor resonators [38, 39].

III. C-QED MODEL OF TWO RESONATORS COUPLED TO THE SAME TLS

A. Theoretical Model

For a theoretical model of the DURKID, we use a standard quantum information science method (c.f. Ref. [40]). Fig. 4(a) shows the system diagram for the model, which has two resonator modes. We describe it with two resonator modes, each with its own two-port transmission line. Both modes are simultaneously coupled to a TLS noise source. Only one TLS and coupling is shown, but the model generally has TLSs which have different effective couplings to a hybridized resonator mode, due to their symmetry created by inter-resonator mode coupling Ω_{AB} . κ_A and κ_B are the coupling rates of resonators A and B, respectively, to their intended 2-port transmission line. The coupling rates of the resonators to the other (unintended) transmission lines are represented by κ_{Ax} and κ_{Bx} , respectively. In this analysis we focus on TLSs that are far enough from resonance to not be saturated by the drive field. A coupled TLS pair could cause a different qualitative noise spectra (c.f. Ref. [19]), but also the method of protection is qualitative and thus the interaction within a capacitor should not matter. Generally we consider that the resonators are coupled to the i -th TLS with a resonance coupling constant of g_i . We represent the TLSs by the spin operator σ_i^z due to the standard analogy between TLS theory and a two state system (with pseudo spin- $\frac{1}{2}$). The Hamiltonian for the system interacting with two transmission lines has the form

$$\begin{aligned}
 H_{sys} = & \hbar\omega_A a^\dagger a + \hbar\omega_B b^\dagger b + \sum_{i=1}^N \varepsilon_i \sigma_i^z + \sum_{j=1}^M \varepsilon_j \sigma_j^z \\
 & + \hbar\Omega_{AB}(b^\dagger a + a^\dagger b) \\
 & - i\hbar \sum_{i=1}^N g_i^{(n)} (\sigma_i^+(a + b) + \sigma_i^-(a^\dagger + b^\dagger)) \\
 & - i\hbar \sum_{j=1}^M g_j^{(m)} (\sigma_j^+(a - b) + \sigma_j^-(a^\dagger - b^\dagger)),
 \end{aligned} \tag{1}$$

this is similar to the one-cavity Jaynes-Cumming Hamiltonian model, which unlike the standard Jaynes-Cummings Hamiltonians [41–44], includes 2 modes (with operators a and b) with many TLSs (with raising and

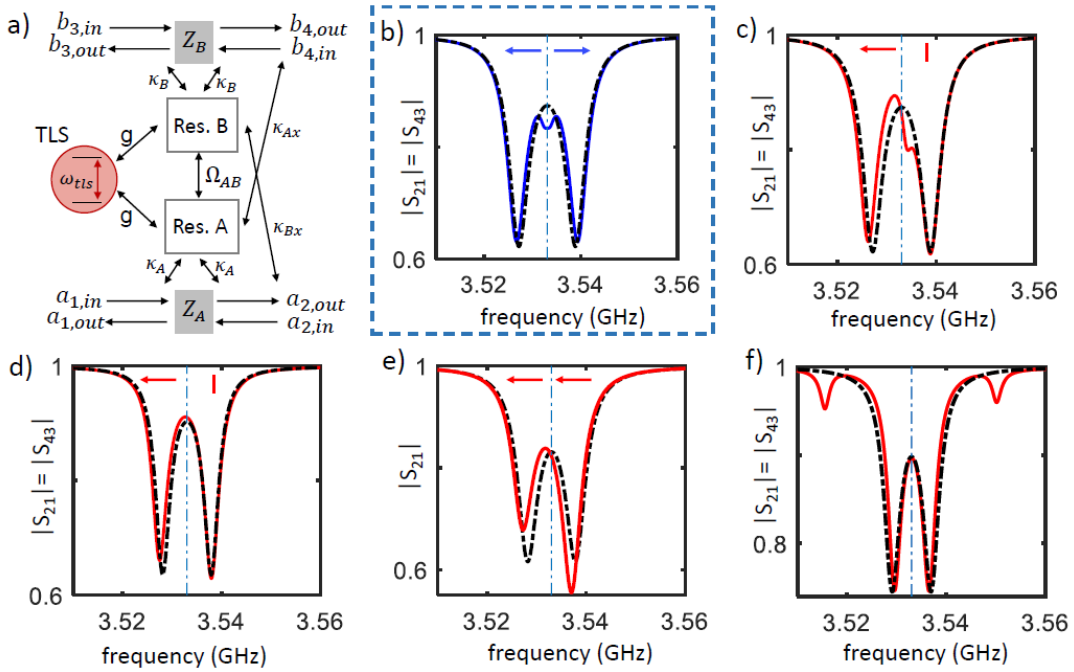


FIG. 4. (a) Theoretical model for the DuRKID, including 2 resonators, 4 ports (fully shown), and TLSs (only 1 TLS shown). In this simulation, the coupling parameters are $\kappa_A/2\pi = \kappa_B/2\pi = 2 \text{ MHz}$, $\gamma_{TLS}/2\pi = 2 \text{ MHz}$, $\Omega_{AB}/2\pi = 5 \text{ MHz}$ and $g/2\pi = 1 \text{ MHz}$. Resonator A is intentionally coupled to transmission line of port (1) and (2), and resonator B to port (3) and (4). (b-f) Transmission analysis for $(1 \rightarrow 2 \text{ or } 3 \rightarrow 4)$ with $Z_A, Z_B \rightarrow 0$ (zero impedance between transmission line halves). Arrows (red or blue) show resonator mode frequency (solid curve transmission minima) change due to the TLS, relative to the mode frequency without the TLS (dashed curve transmission minima). (b-c) Single-photon transmission spectrum for two different devices with same parameters, ($\omega_A/2\pi = \omega_B/2\pi = 3.533 \text{ GHz}$) with a single degenerate TLS ($\omega_{TLS} = \omega_A = \omega_B$). (b) Standard-coupled resonators which are hybridized. Note that the frequency shift (dispersion) occurs equally (correlated) in both modes (blue relative to black minima, also see blue arrows). (c) DuRKID in intended (hybridized) mode with a TLS. Here the TLS leaves one of the modes undispersed. (d) DuRKID with a large drive (classical field) amplitude of $\bar{n} = 50$ photons and a TLS frequency of $\omega_{TLS}/2\pi = 3.540 \text{ GHz}$. Here the dispersion is present, related to (c), and the TLS is symmetry-protected from saturation. Undispersing modes occur in DuRKID due to the absence of fields in certain capacitors according to the symmetry of the hybridized modes (see Figure 1(b)). (e) The spectra for the bridge-type resonator device in the presence of an added signal to one inductor (in contrast to other sub-figures which use additional TLS(s)). Here the hybridization of the modes change as seen in different resonator transmission amplitudes. The resonator frequency modes shift downward together (as correlated modes), in contrast to the case of single-TLS perturbation (c or d). (f) Spectra with two TLSs, where there is one from each group (where each mainly influences only one of the resonator modes). This case is used in section III B, for analysis with two TLS noise sources. A TLS in each TLS group disperses each hybridized mode, but it is distinguishable from the (correlated-mode) signal. In this special case there is no change of mode hybridization due to the way that the TLSs oppositely disperse (shift) the resonator modes.

lowering operators σ_i^+ and σ_i^-). The i th TLS has energy of $\varepsilon_i = \frac{\hbar\omega_{TLS,i}}{2} = \sqrt{\Delta_i^2 + \Delta_{0,i}^2}$, where Δ_0 and Δ are tunneling energy and the asymmetry energy in the double-well potential model. TLS resonance coupling to the resonator field is $g_i = \frac{\Delta_{0,i}}{\varepsilon_i} p_i \cos\theta_i \sqrt{\frac{\omega}{2\epsilon_r \epsilon_0 \hbar V}}$, where p_i is the magnitude of the dipole moment, θ_i is the angle between p_i and the applied electric field \mathbf{E} , V is the dielectric volume, and ϵ_r is the relative permittivity [45]. Though a given TLS in a capacitor is equally shared by both modes before hybridization, after hybridization the two mode fields become $E_+ \propto (a + b)$ and $E_- \propto (a - b)$, which are zero in certain capacitors as mentioned above. It becomes zero in 2 of the capacitors for one hybridized

mode and similarly zero in the other 2 capacitors of the other hybridized mode. We find that this approximation is valid even for a TLS throughout the eigenmode width. For the two modes we thus effectively have only the coupling to N TLSs (group n) in capacitor pair C_1, C_3 , and M TLSs (group m) in C_2, C_4 . Using a standard theoretical procedure [46] for the resonators A and B, interacting with the input and output fields as the heat bath, the

Heisenberg equations of motion can be written as:

$$\begin{aligned} \frac{d}{dt} \langle a \rangle = -i\omega \langle a \rangle &= -\frac{i}{\hbar} \langle [a, H_{sys}] \rangle - (\kappa_A + \gamma_A + \kappa_{Ax}) \langle a \rangle \\ &+ \sqrt{\kappa_A} \langle a_{1,in} \rangle + \sqrt{\kappa_A} \langle a_{2,in} \rangle + \sqrt{\kappa_{Ax}} \langle b_{3,in} \rangle \\ &+ \sqrt{\kappa_{Ax}} \langle b_{4,in} \rangle - \sqrt{\kappa_A \kappa_{Bx}} \langle b \rangle - \sqrt{\kappa_{Ax} \kappa_B} \langle b \rangle, \end{aligned} \quad (2)$$

$$\begin{aligned} \frac{d}{dt} \langle b \rangle = -i\omega \langle b \rangle &= -\frac{i}{\hbar} \langle [b, H_{sys}] \rangle - (\kappa_B + \gamma_B + \kappa_{Bx}) \langle b \rangle \\ &+ \sqrt{\kappa_B} \langle b_{3,in} \rangle + \sqrt{\kappa_B} \langle b_{4,in} \rangle + \sqrt{\kappa_{Bx}} \langle a_{1,in} \rangle \\ &+ \sqrt{\kappa_{Bx}} \langle a_{2,in} \rangle - \sqrt{\kappa_B \kappa_{Ax}} \langle a \rangle - \sqrt{\kappa_{Bx} \kappa_A} \langle a \rangle, \end{aligned} \quad (3)$$

where $a_{1,(2),in}, b_{3,(4),in}$ and $a_{1,(2),out}, b_{3,(4),out}$ are the input and output fields. Assuming a coherent-state approximation for photons in resonators A and B coupled to input and output fields, the transmission S_{21} and S_{43} are given by $\frac{\langle a_{2,out} \rangle}{\langle a_{1,in} \rangle}$ and $\frac{\langle b_{4,out} \rangle}{\langle b_{3,in} \rangle}$, respectively. The boundary conditions which relate the input and output fields

to photon annihilation in each resonator, $a_{1,(2),out} = \sqrt{\kappa_A}a - a_{2,(1),in} + \sqrt{\kappa_{Bx}}b$ and $b_{3,(4),out} = \sqrt{\kappa_B}b - b_{4,(3),in} + \sqrt{\kappa_{Ax}}a$, are used in the analysis [46]. We assume only one input field $a_{1,in}$ (i.e. $a_{2,in} = b_{4,in} = b_{3,in} = 0$) is present for S_{21} and $b_{3,in}$ (i.e. $a_{2,in} = b_{4,in} = a_{1,in} = 0$) for S_{43} . The details of theoretical analysis are described in Appendix B.

We next confine ourselves to degenerate modes $\omega_A = \omega_B = \omega_r$, and, for simplicity, M-group TLSs (which belong to the capacitor pair labeled with m). We can see from the Hamiltonian that for positive Ω_{AB} the M TLSs are interacting with the lower frequency mode. We also reduce the calculation to equal coupling and photon decay rates in each resonator: $\kappa_A = \kappa_B = \kappa_r, \gamma_A = \gamma_B = \gamma_r$, and assume each resonator is decoupled from the other transmission line, $\kappa_{Ax} = \kappa_{Bx} = 0$. In the low-temperature and low-drive power limit ($k_B T \ll \hbar\omega$ and $n_{ph} \ll 1$), the resonator will be asymptotically close to the ground state and we find the transmission amplitude of this four-port system as

$$S_{43} = S_{21} = 1 - \kappa_r \frac{-i(\omega - \omega'_r) + \kappa_r + \gamma_r}{-(\omega - \omega'_r)^2 + (\kappa_r + \gamma_r)^2 - (i\Omega_{AB} - \sum_i^M \frac{\tanh(\frac{\hbar\omega}{2k_B T})g_i^2}{\frac{\hbar\omega}{2k_B T} + \frac{\gamma_i^2}{2}})^2 - 2i(\kappa_r + \gamma_r)(\omega - \omega'_r) - i(\omega - \omega_{TLS}^i) + \frac{\gamma_{TLS}^i}{2}}, \quad (4)$$

where $\omega'_r = \omega_r - \sum_i^M \frac{\tanh(\frac{\hbar\omega}{2k_B T})g_i^2}{\omega - \omega_{TLS}^i + i\frac{\gamma_{TLS}^i}{2}}$. In the Appendix, we provide the transmission for TLSs interacting with the high-frequency mode (Eq. 19) and that of the standard-coupled resonator pair (Eq. 24), as well as the cross transmission from port 3 to 2 (S_{23}) and from port 1 to 4 (S_{41}), with non-zero (finite) κ_{Ax} and κ_{Bx} (Eqs. 18, 19).

B. Theoretical Results

In order to investigate the effect of TLS noise on the two resonator modes, we use the analytical results derived from Eq. (4) for both transmission lines in the limit of a weakly coupled TLS where $g \ll \Omega_{AB}$. The system we consider is shown in Fig. 4(a). Figs. 4(b) and (c) show the spectra of transmission $|S_{21}|$ for a TLS with the uncoupled modes in the standard-coupled design and the DuRKID, respectively. As shown, a given TLS in the DuRKID generally only shifts one of the two hybridized modes (Fig. 4(c)), as expected. This is true even for a TLS that is detuned from the coupled modes (related to hybridized mode symmetries). In contrast, a TLS in either capacitor in the standard degenerate design will couple with equal strength to the two modes and cause a frequency shift to both (see Fig. 4(b)). The difference is evident from the TLS-resonator interaction term in Eq. (1) which differs from the standard-coupled resonators (see Eq. 24 in the Appendix). Thus the DuRKID has

single-mode noise for a single TLS, whereas a standard-coupled TLS has correlated-mode noise (see Appendix B for more data on the off-resonance TLS case). We also consider the case of strong readout tone from port 1 or 3 (see also Appendix A). In Fig. 4(d) the transmission spectra is shown in the presence of strong pump drive with $H_d = i\hbar\sqrt{\kappa_A}A(t)a^\dagger$, where $\langle a_{1,in}(t) \rangle = A(t)$ and $\langle a_{2,in}(t) \rangle = \langle b_{3,in}(t) \rangle = \langle b_{4,in}(t) \rangle = 0$. As shown, a given TLS in the bridge capacitor design, even in the presence of the strong pump drive, only shifts one of the two hybridized modes. Figure 4(e) shows the simulated signal on both resonance modes in the bridge resonator design viewed from transmission spectra $1 \rightarrow 2$ (with $Z_A, Z_B \rightarrow 0$). Specifically, the solid line shows the transmission with a signal that increases L_B , as expected for a KID. We see relative to the unperturbed transmission (the dashed line) that the transmission spectra has a shift in both resonance modes to lower frequency, as expected from earlier arguments. In addition, the relative size of the observed transmission notches are changed due to the way the modes are changed qualitatively – one mode is more A-like, just as the other mode is more B-like. In summary, one DuRKID mode will experience frequency shifts from one set of capacitors (m-group TLSs in equation 4) that will shift a single mode; this is distinguishable from two correlated modes caused by the signal.

Figure 4(f) shows the transmission spectra of the DuRKID in the presence of two TLSs, one from each group (capacitor pair). Next this arrangement with two

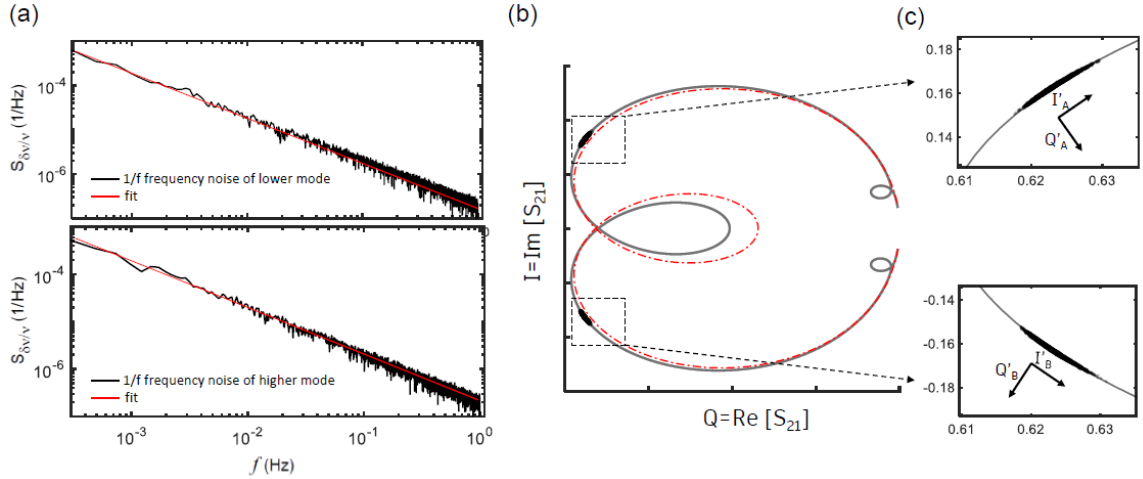


FIG. 5. Noise analysis for $1/f^\alpha \sim 1/f$ TLS noise, using time-domain simulations for two variable-frequency TLSs. (a) Fractional frequency noise spectral density $S_{\delta\nu/\nu}$ for the two resonator modes. Solid line is a fit to $A/[f/(1\text{Hz})] + B$, where here we define A as the $1/f$ noise density and B for the white noise density. (b) Complex transmission, $\text{Im}[S_{21}]$ versus $\text{Re}[S_{21}]$, for the DuRKID with two TLSs (black line), where there is one TLS from the m and n groups, which according to the design implies that each TLS couples to only one mode. The red dashed line is shown for the transmission without TLSs (this was numerically obtained with zero TLS coupling, which is equivalent). The solid and dashed lines are can be compared to transmission magnitude versus frequency, Fig. 4(f), where there are 4 minima in the case of coupled TLSs. Transmission time-domain simulation at 2 fixed input frequencies (black points in 2 dashed boxes). The 2 sets of accumulated points are further apart in I than the Q minima (solid line) because the input frequencies for TLS noise analysis were chosen to be equal to the case without coupled TLS, and as Fig. 4(f) shows: the resonance minima for the case with TLS (solid line of Fig. 4(f)) are closer in frequency than the case without TLS coupling (dashed line Fig. 4(f)). (c) Zoomed view of transmission points accumulated in time for fixed input frequencies (black points). The transmission for various frequencies is shown as a grey line. (upper panel) I'_A quadrature defined as the tangent of the transmission versus frequency on the 1st mode. (lower panel) I'_B quadrature defined as the tangent of the transmission versus frequency on the 2nd mode. Noise in the resonator modes is uncorrelated due to separated noise sources, unlike the signal in the KID (see Appendix B section 3).

TLSs is used to calculate the cross-spectral density with TLSs and the two noise sources. For this we simulate the TLS-induced frequency noise of two resonator modes split by Ω_{AB} , with bare resonance frequencies of $\omega_0/2\pi = 3.533$ GHz. The frequency noise spectral density $S_{\delta\nu/\nu}(f)$ is simulated with one TLS from each TLS group (m or n), by setting a $1/f$ noise spectrum on each. In Fig. 5(a), we show the simulated frequency-noise spectral density for resonators A and B. TLS frequency fluctuations in turn create fluctuations on the resonator modes, according to their effective couplings. The TLS with higher energy is coupled to the higher resonator mode while the lower energy TLS is coupled to the lower mode. These conditions create uncorrelated $1/f$ frequency noise in the resonator modes (see Appendix B). $\text{Im}[S_{21}]$ versus $\text{Re}[S_{21}]$ is shown in Fig. 5(b) and (c) without any TLSs interaction, $g = 0$, (red line) and the TLSs interaction (grey line). Even though we have not analyzed more TLSs, from the principle of superposition we can expect the uncorrelated noise feature will continue for a typical TLS distribution – TLSs noise should not be correlated in separate capacitors. This is distinct from correlated noise in the modes, which exists only where expected (See Appendix).

C. Discussion

The most straightforward analysis of the system uses one feedline, e.g., ports 1 and 2. This corresponds to simulated data of S_{21} shown in Fig. 5(c). The advantage of the method is sufficient for TLS noise distinction and in a future version of the DuRKID one may choose to eliminate the second feedline. However, one could instead measure with 2 feedlines, where each feedline measures one resonator. In this case, when a signal perturbs the frequencies, each resonator signal could be equal in magnitude as each mode takes on an emphasized character of one of the physical resonator modes. We also measured unintended leakage (crosstalk) between the two different feedlines at $|S_{14}| \sim 10^{-4}$ (this was measured with resonators detuned to see the stray coupling near either the A or B resonator mode. From this we extracted the couplings of the resonators to the unintended feed lines as $\kappa_{ax} = \kappa_{bx} \sim 20$ kHz (see Appendix).

We specified a TLS noise mitigation technique for ideal fabrication, where the hybridized mode noise is perfectly uncorrelated. However, noise sources can become correlated if the capacitor bridge is asymmetric, or if the inter-resonator coupling becomes too small to create dis-

tinction of the modes. In practice, there will be some correlation between the components even in an optimal experimental circuit due to measurement noise and factors that were not addressed above. Thus in the future, one may want to construct an optimal linear filter based on the correlations and other noise mechanisms (white noise from amplifiers included, for example). In one approach for this, the optimal linear filter can be computed by measuring the 4-component noise and then computing the cross-spectral density matrix (see Eqs. 13 and 16 in Ref. [47]).

IV. CONCLUSION

In summary, we have proposed a new KID detector prototype consisting of two superconducting circuit resonators. We first described the fabricated device and schematic consisting of two resonators that both share an electrical capacitance bridge. We then showed the basic transmission and fittings of the device data along with frequency tuning of one mode which is necessary for device operation. $1/f$ noise will naturally arise from TLSs in the dielectric of the capacitors, as found in previous studies. In our study the capacitor configuration in the device allows the two resonators to share common TLSs generally, but this changes once the resonators are tuned to degeneracy, where a given TLS only perturbs one of the two hybridized resonator modes due to its residency in one of two TLS groups (n or m). This leads to uncorrelated noise in the two resonator modes since they experience separate noise sources.

We performed transmission measurements on the DuRKID and found experimentally that the coupling between the modes is larger than the coupling of a TLS to a resonator mode. Furthermore, to achieve degeneracy, we tuned a resonators by up to 120 MHz with an applied current. To show that any given TLS will be coupled to only one of the two fully hybridized modes, we then analyzed the device schematic theoretically using a model with 4 ports coupled to 2 resonators, where a representative TLS of each TLS group resides in the bridge. The simulation shows that TLS noise is different than the intended KID signal. From the transmission data we obtain the TLS loss tangents, inter-resonator coupling, and the intended and unintended couplings to transmission lines.

In the future, we plan to demonstrate the uncorrelated noise in the device from TLSs. In principle the measurement can be made by monitoring the lack of correlation over time while the resonator pair is near the fully hybridized state. We specify the TLS noise mitigation technique in terms of 2 quadratures of resonator transmission measurements of amplitude and phase at 2 frequencies (4 components) of the DuRKID. The noise from the hybridized state can be compared when the res-

onators are non-hybridized, where the noise from TLSs should appear as correlated noise on the resonators.

ACKNOWLEDGMENTS

The authors thank F. C. Wellstood, C. Richardson, R. Ruskov and W. Wustmann for scientific discussions. This work was funded through a NASA Science Innovation Fund (SIF) award and the Intelligence Community Postdoctoral Fellowship Award.

APPENDIX A: NONLINEARITY OF THE KINETIC INDUCTANCE AND THE FITTING PROCEDURE

1. Nonlinearity of the kinetic inductance

As described in the main text, the inductance of the LC resonators is made tunable with DC bias. We measured the nonlinearity explicitly in device 2 at milliKelvin temperature with a direct applied bias current (note that device 1 and 3 share a single dc-input current in parallel). The relationship was given previously for inductance as a quadratic function of bias current, but here we describe the nonlinear inductance. The TiN inductor width is 5 mm wide. Fig. 6(a) shows frequency of the resonator as a function of bias current squared. The fractional resonance frequency shift can be written in terms of current or inductance as:

$$\frac{\delta f_r}{f_r} = -\frac{I_b^2}{2I'^2} = -\frac{\delta L_r}{2L_r}. \quad (4)$$

We fit to a quadratic model as a function of bias current I_b as shown in Fig. 6(a) and from this extracted $I' = 789 \mu\text{A}$. In Fig. 6(b) we show the same type of fit, except using inductance as the independent variable rather than the frequency.

2. The fitting procedure

In order to fit the measured complex transmission data, S_{21} , S_{43} and S_{31} we use Eqs. (18), (19) and (20). Although general formulas can be made to directly fit for the many parameters simultaneously, such multi-parameter fitting problems can be extremely sensitive to the initial values due to the local optimization of the parameters, and different amounts of noise in different data sets. Fitting a small subset of the data leads to under determined constraints and inaccuracies due to covariances. To resolve this issue, we utilize an iterative procedure through which our fitting problem, with 10-parameters, is broken down into several independent fitting problems

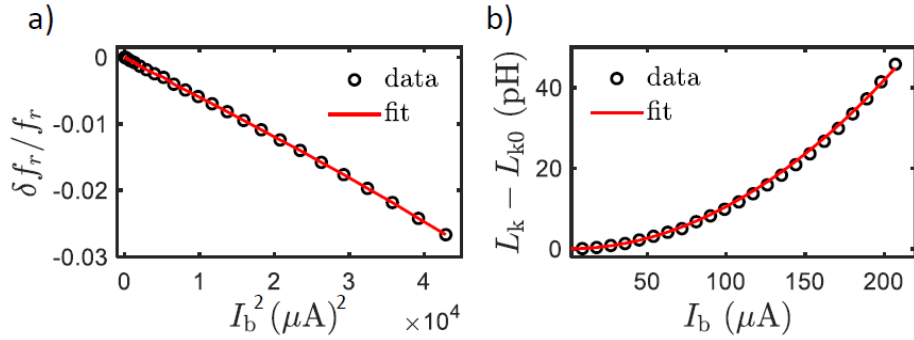


FIG. 6. a) Frequency and b) kinetic inductance dependence on I_b .

with carefully chosen fixed parameters. Each fit contains only a few (two or three) parameters at a time. First we extract the cross coupling Ω_{AB} from the data of Fig. 3(c). We have previously performed resonator fittings from transmission data (e.g., S_{21}) using the diameter correction method (DCM) (for a single resonator) [48]. This technique uses a Least-Squares Monte Carlo (LSM) method to find the minimum error, χ^2 . To fit both S_{21} and S_{43} we developed a fitting sequence using a sequence of different LSM fittings in multi-step procedure. We start by using LSM fitting primarily with S_{21} data, using device model (equation (18)), except that an extra multiplicative factor $e^{i\theta}$ is applied to the right hand side of Eq. (18) to account for the transmission line length. Initial guesses must be placed for all variables, including $\omega_A, \omega_B, \kappa_A, \kappa_B, \gamma_A, \gamma_B, \kappa_{Ax}, \kappa_{Bx}$. Within the LSM fitting a Monte Carlo guess is made in the form $x = x_0 e^{\zeta \xi}$ for each fit parameter, where x_0 is the previous (initial) guess for the fit parameter x , ζ is a randomly generated number between -1 and 1, and ξ is a parameter smaller than one, that determines the MC guess domain.

However, to optimize S_{21} in the first fit we use two different ξ for the different parameters. For parameters associated with resonator B, we use fast iterations e.g. using $\xi = 0.1$ for $\omega_A, \kappa_A, \gamma_A, \kappa_{Ax}, \theta_{21}$ to optimize it quickly. Meanwhile, for parameters associated with resonator A, we use slow iterations, e.g., using $\xi = 10^{-5}$ for $\omega_B, \kappa_B, \gamma_B, \kappa_{Bx}, \theta_{43}$, to leave the parameters with

only slight changes. After this step, the updated values are used to fit S_{43} following the same procedure, with the difference that this time the variation of resonator A parameters are quickly optimized and resonator B parameters are mainly left unchanged. Next the S_{43} fit parameters are determined, such that S_{21} could be fit, and this completes one cycle of our procedure. The previous 2 steps are repeated in sequence: for example by using the fit results from S_{21} (S_{43}) we then fit S_{43} (S_{21}). The cycles of fitting are then repeated iteratively for many times until convergence is obtained. The standard resonator coupling to the intended transmission line is $Q_c^{A,B} = \frac{\omega_{A,B}}{2\kappa_{A,B}}$. The internal loss from one resonator is often desired, which is $Q_i = \frac{\omega}{\gamma}$ in our devices, where the resonator loss $1/Q_i$ is due to the sole dielectric in each resonator. Since we have dual transmission line setup, it is useful to define the apparent internal quality factor for each resonator $Q_{i,app}^{A,B} = \frac{\omega_{A,B}}{\gamma_{A,B} + 2\kappa_{Ax,Bx}}$, which not only depends on the internal loss rate of the resonator to its internal loss $\gamma_{a,b}$, but also the coupling loss to the unintended transmission line $2\kappa_{Ax,Bx}$, respectively. Figure 7 (a) and (b) show an example of such a fit to two resonance lineshapes for resonators A and B which are coupled to transmission lines 1-2 and 3-4 respectively for -140 dB power at device. The extracted fitting parameters from S_{21} and S_{43} are used as an initial guess to fit the cross transmission from port 1 to 4, S_{41} .

APPENDIX B: DERIVATION OF THE TRANSMISSION FOR TWO RESONANCES INTERACTING WITH TLS

1. LC resonator pair with an internal electrical bridge of capacitors

The system we consider in Fig. 1(a) consists of two resonators and TLSs, described by the Hamiltonian H_{sys} (Eq. 2). It is coupled to 2 transmission lines that are accessible at their ends via 4 ports. The system has resonator modes a and b. According to the standard theory of input and output for quantum dissipative systems [40], the transmission lines can be modeled as a heat bath. Additionally, the couplings can be specified between transmission lines and the intended couplings, κ_A and κ_B , as well as the unintended couplings, κ_{Ax} and κ_{Bx} . The Heisenberg equation of motion for the bare resonator modes in terms of the system and input-output fields can be written as Eq. (2), (3),

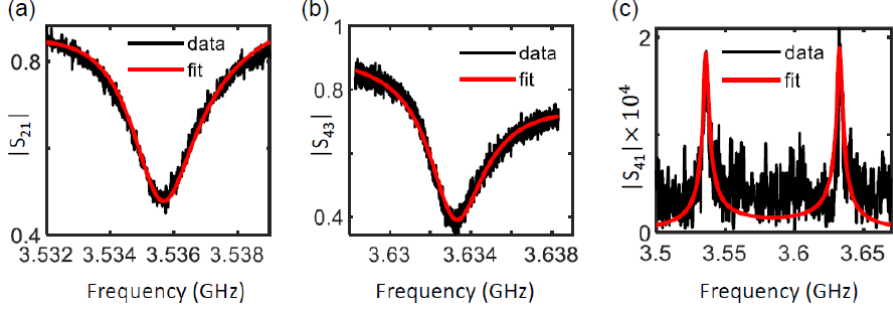


FIG. 7. Transmission data in the absence of bias for resonator A (a) and resonator B (b). The red curves show the fit of data to the model. The fit yielded $\omega_A = 3.5357$ GHz, $\gamma_A = 0.88$ MHz, $\kappa_A = 0.9$ MHz, $\kappa_{Ax} = 20$ kHz, and $\omega_B = 3.6335$ GHz, $\gamma_B = 0.77$ MHz, $\kappa_B = 1.01$ MHz, $\kappa_{Bx} = 19.7$ kHz, $Q_i^A = 2741$, $Q_i^B = 3026$ and $Q_c^A = 1930$, $Q_c^B = 1800$. (c) Crosstalk coupling (unintended coupling) between port 1 and 4 of device two in the absence of bias. Fitting data gives 20.3 kHz of cross coupling between port 1 and 4 with $\omega_A = 3.534$ GHz, $\gamma_A = 0.91$ MHz, $\kappa_A = 0.97$ MHz, $\kappa_{Ax} = 20.3$ kHz, and $\omega_B = 3.6335$ GHz, $\gamma_B = 0.77$ MHz, $\kappa_B = 1.01$ MHz, $\kappa_{Bx} = 19.5$ kHz. Agreement between data and 4-port model confirms appropriateness of the fit method and the many parameter model.

$$\frac{d}{dt} \langle a \rangle = -i\omega \langle a \rangle = -\frac{i}{\hbar} \langle [a, H_{sys}] \rangle + \kappa_A \langle a \rangle - \sqrt{\kappa_A} \langle a_{1,out} \rangle - \sqrt{\kappa_A} \langle a_{2,out} \rangle - \sqrt{\kappa_{Ax}} \langle b_{3,out} \rangle - \sqrt{\kappa_{Ax}} \langle b_{4,out} \rangle - \gamma_A \langle a \rangle + \kappa_{Ax} \langle a \rangle + \sqrt{\kappa_A \kappa_{Bx}} \langle b \rangle + \sqrt{\kappa_{Ax} \kappa_B} \langle b \rangle, \quad (5)$$

and

$$\frac{d}{dt} \langle b \rangle = -i\omega \langle b \rangle = -\frac{i}{\hbar} \langle [b, H_{sys}] \rangle + \kappa_B \langle b \rangle - \sqrt{\kappa_B} \langle b_{3,out} \rangle - \sqrt{\kappa_B} \langle b_{4,out} \rangle - \sqrt{\kappa_{Bx}} \langle a_{1,out} \rangle - \sqrt{\kappa_{Bx}} \langle a_{2,out} \rangle - \gamma_B \langle b \rangle + \kappa_{Bx} \langle b \rangle + \sqrt{\kappa_B \kappa_{Ax}} \langle a \rangle + \sqrt{\kappa_{Bx} \kappa_A} \langle a \rangle. \quad (6)$$

We write the equation of motion for the TLS operator σ_i^- for TLS ‘i’ using the Bloch equations approximation for relaxation and decoherence

$$\frac{d}{dt} \langle \sigma_i^- \rangle = -i\omega \langle \sigma_i^- \rangle = -i\omega_{TLS,i} \langle \sigma_i^- \rangle - \frac{\gamma_{TLS,i}}{2} \langle \sigma_i^- \rangle + 2g \langle \sigma_i^z a \rangle + 2g \langle \sigma_i^z b \rangle, \quad (7)$$

where the TLS decoherence rate is $\gamma_{TLS,i} = k_{1,i} + 2k_{2,i}$, where typically $k_{1,i} = A_1 \Delta_{0,i}^2 \coth(\frac{\hbar\omega}{2k_B T})$ and $k_{2,i} \approx A_2 T^2$. The rates $k_{1,i}$ and $k_{2,i}$ describe TLS *i* relaxation and phase decoherence rates associated with TLS-photon and TLS-TLS interactions, respectively and A_1 and A_2 are material related constants [49]. In the low-temperature and low-drive power limit ($k_B T \ll \hbar\omega$ and $n_{ph} \ll 1$), the resonator will be asymptotically close to the ground state. This suggests that we can replace the spin operator $\langle \sigma_i^z \rangle$ in Eq. (6) with the ground state value $-\frac{1}{2}$. With these assumptions we obtain a closed system of linear equations which can be solved for the TLS operators:

$$\langle \sigma_i^- \rangle = \frac{2g(\langle a \rangle + \langle b \rangle) \langle \sigma_i^z \rangle}{i(\omega_{TLS,i} - \omega) + \frac{\gamma_{TLS,i}}{2}}. \quad (8)$$

For thermally excited TLS, one can use a mean field approach replacing the operator $\langle \sigma_i^z \rangle$ in Eq. (6) with its thermodynamic average value, i. e. $\langle \sigma_i^z \rangle_{th} = -\frac{1}{2} \tanh(\frac{\hbar\omega}{2k_B T})$. This approach is consistent with previous analysis of sound and microwave absorption by TLSs [50, 51]. The average value of $\langle \sigma_i^z \rangle$ at higher photon regime is calculated in the next section. To proceed, we now substitute the solution for $\langle \sigma_i^- \rangle$ (Eq. 8) into Eqs. (2-4) and obtain the solution for resonator mode *a* and *b*:

$$L_{A,+} \langle a \rangle + L_{AB,+} \langle b \rangle = \sqrt{\kappa_A} \langle a_{1,in} \rangle + \sqrt{\kappa_A} \langle a_{2,in} \rangle + \sqrt{\kappa_{Ax}} \langle b_{3,in} \rangle + \sqrt{\kappa_{Ax}} \langle b_{4,in} \rangle, \quad (9)$$

$$L_{A,-} \langle a \rangle + L_{AB,-} \langle b \rangle = -\sqrt{\kappa_A} \langle a_{1,out} \rangle - \sqrt{\kappa_A} \langle a_{2,out} \rangle - \sqrt{\kappa_{Ax}} \langle b_{3,out} \rangle - \sqrt{\kappa_{Ax}} \langle b_{4,out} \rangle, \quad (10)$$

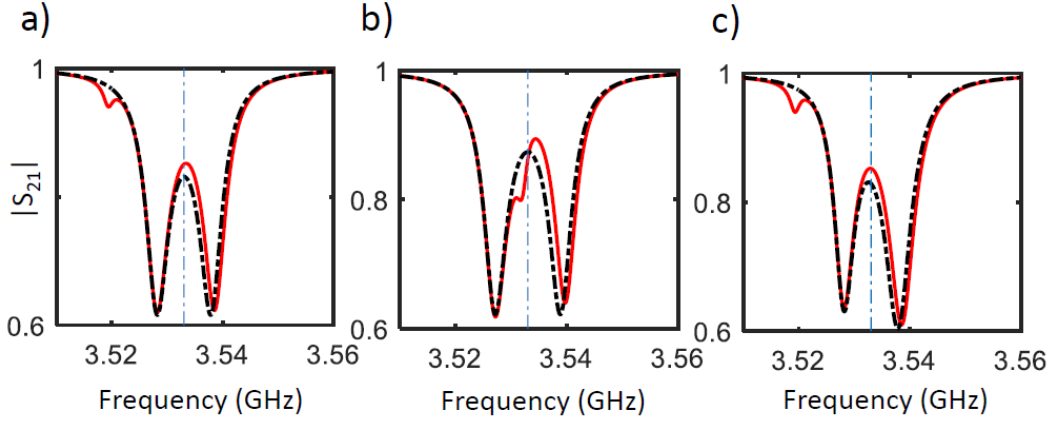


FIG. 8. a) Simulated transmission magnitude $|S_{21}|$ (with $Z_B \rightarrow 0$) for a single TLS off resonance coupled to a+b field in the bridge design. The TLS frequency of $\omega_{tls} = 3.52$ GHz is used here and the rest of parameters are the same as before. Note that dispersion is not caused at the neighboring frequency mode, but at the mode that has the proper coupling for the TLSs capacitor. b) The impact of a single TLS on resonance coupled to a+b field on both hybridized modes. c) The impact of non zero unintended coupling of each resonator to the other transmission line, $\kappa_{Ax} = \kappa_{Bx} = 20$ kHz for data presented in (a).

$$L_{B,+} \langle b \rangle + L_{AB,+} \langle a \rangle = \sqrt{\kappa_B} \langle b_{3,in} \rangle + \sqrt{\kappa_B} \langle b_{4,in} \rangle + \sqrt{\kappa_{Bx}} \langle a_{1,in} \rangle + \sqrt{\kappa_{Bx}} \langle a_{2,in} \rangle, \quad (11)$$

$$L_{B,-} \langle b \rangle + L_{AB,-} \langle a \rangle = -\sqrt{\kappa_B} \langle b_{3,out} \rangle - \sqrt{\kappa_B} \langle b_{4,out} \rangle - \sqrt{\kappa_{Bx}} \langle a_{1,out} \rangle - \sqrt{\kappa_{Bx}} \langle a_{2,out} \rangle, \quad (12)$$

where,

$$L_{A,\pm} = -i\omega + i\omega_A + \gamma_A \pm \kappa_A \pm \kappa_{Ax} - \sum_{i=1}^N \frac{2sg_i^2}{i(\omega_{TLS,i} - \omega) + \frac{\gamma_{TLS,i}}{2}}, \quad (13)$$

$$L_{AB,\pm} = i\Omega_{AB} \pm \sqrt{\kappa_A \kappa_{Bx}} \pm \sqrt{\kappa_{Ax} \kappa_B} - \sum_{i=1}^N \frac{2sg_i^2}{i(\omega_{TLS,i} - \omega) + \frac{\gamma_{TLS,i}}{2}}, \quad (14)$$

$$L_{B,\pm} = -i\omega + i\omega_B + \gamma_B \pm \kappa_B \pm \kappa_{Bx} - \sum_{i=1}^N \frac{2sg_i^2}{i(\omega_{TLS,i} - \omega) + \frac{\gamma_{TLS,i}}{2}}. \quad (15)$$

To study one coherent input, we then set $\langle a_{2,in} \rangle = \langle b_{4,in} \rangle = \langle b_{3,in} \rangle = 0$ to calculate S_{21} and $\langle a_{2,in} \rangle = \langle b_{4,in} \rangle = \langle a_{1,in} \rangle = 0$ to calculate S_{43} . The solution for the resonator modes a and b takes the form

$$\langle a \rangle = \frac{\sqrt{\kappa_A} - \frac{L_{AB,+} + \sqrt{\kappa_{Bx}}}{L_{B,+}}}{L_{A,+} - \frac{L_{AB,+}^2}{L_{B,+}}} \langle a_{1,in} \rangle, \quad (16)$$

and

$$\langle b \rangle = \frac{\sqrt{\kappa_{Bx}}}{L_{B,+}} \langle a_{1,in} \rangle - \frac{L_{AB,+}}{L_{B,+}} \frac{\sqrt{\kappa_A} - \frac{L_{AB,+} + \sqrt{\kappa_{Bx}}}{L_{B,+}}}{L_{A,+} - \frac{L_{AB,+}^2}{L_{B,+}}} \langle a_{1,in} \rangle. \quad (17)$$

Using the boundary conditions, $a_{1,(2),out} = \sqrt{\kappa_A}a - a_{2,(1),in} + \sqrt{\kappa_{Bx}}b$ and $b_{3,(4),out} = \sqrt{\kappa_B}b - b_{4,(3),in} + \sqrt{\kappa_{Ax}}a$, and

Eq. (14) and (15), we obtain $S_{21} = \frac{\langle a_{2,out} \rangle}{\langle a_{1,in} \rangle}$, $S_{43} = \frac{\langle b_{4,out} \rangle}{\langle b_{3,in} \rangle}$ and $S_{41} = \frac{\langle b_{4,out} \rangle}{\langle a_{1,in} \rangle}$ as

$$S_{21} = 1 - \frac{\kappa_A}{-i(\omega - \omega_A) + \kappa_A + \gamma_A - \sum_{i=1}^N \frac{2Sg_i^2}{-i(\omega - \omega_{TLS}^i) + \frac{\gamma_{TLS}^i}{2}} - \frac{(i\Omega_{AB} - \sum_{i=1}^N (\frac{2Sg_i^2}{-i(\omega - \omega_{TLS}^i) + \frac{\gamma_{TLS}^i}{2}}))^2}{-i(\omega - \omega_B) + \kappa_B + \gamma_B - \sum_{i=1}^N \frac{2Sg_i^2}{-i(\omega - \omega_{TLS}^i) + \frac{\gamma_{TLS}^i}{2}}}}, \quad (18)$$

$$S_{43} = 1 - \frac{\kappa_B}{-i(\omega - \omega_B) + \kappa_B + \gamma_B - \sum_{i=1}^N \frac{2Sg_i^2}{-i(\omega - \omega_{TLS}^i) + \frac{\gamma_{TLS}^i}{2}} - \frac{(i\Omega_{AB} - \sum_{i=1}^N (\frac{2Sg_i^2}{-i(\omega - \omega_{TLS}^i) + \frac{\gamma_{TLS}^i}{2}}))^2}{-i(\omega - \omega_A) + \kappa_A + \gamma_A - \sum_{i=1}^N \frac{2Sg_i^2}{-i(\omega - \omega_{TLS}^i) + \frac{\gamma_{TLS}^i}{2}}}}, \quad (19)$$

and

$$S_{41} = \frac{\sqrt{\kappa_{Bx}\kappa_B}}{L_{B,+}} - \frac{L_{AB,+}(L_{B,+}\sqrt{\kappa_B\kappa_A} - L_{AB,+}\sqrt{\kappa_B\kappa_{Bx}})}{L_{B,+}(L_{B,+}L_{A,+} - L_{AB,+}^2)} + \frac{\sqrt{\kappa_{Ax}\kappa_A} - \frac{\sqrt{\kappa_{Ax}L_{AB,+}\sqrt{\kappa_{Ax}\kappa_{Bx}}}}{L_{B,+}}}{L_{A,+} - \frac{L_{AB,+}^2}{L_{B,+}}}. \quad (20)$$

Reducing the calculation to equal coupling and photon decay rates for each resonator: $\kappa_A = \kappa_B = \kappa_r$, $\gamma_A = \gamma_B = \gamma_r$, and assuming no (cross) coupling to the unintended transmission line, $\kappa_{Ax} = \kappa_{Bx} = 0$, the transmission properties of this four-port system coupling to a single TLS through the $a + b$ field is given by

$$S_{43} = S_{21} = 1 - \kappa_A \frac{-i(\omega - \omega'_r) + \kappa_r + \gamma_r}{-(\omega - \omega'_r)^2 + (\kappa_r + \gamma_r)^2 - (i\Omega_{AB} - \frac{\tanh(\frac{\hbar\omega}{2k_B T})g^2}{-i(\omega - \omega_{TLS}) + \frac{\gamma_{TLS}}{2}})^2 - 2i(\kappa_r + \gamma_r)(\omega - \omega'_r)}, \quad (21)$$

where $\omega'_r = \omega_r - \frac{g^2}{\omega - \omega_{TLS} + i\frac{\gamma_{TLS}}{2}}$. Similarly, coupling to a single TLS through the $a - b$ field can be obtained.

2. Standard-coupled two-resonator

Considering the standard-coupled two-resonator with Hamiltonian of

$$H_{sys} = \hbar\omega_A a^\dagger a + \hbar\omega_B b^\dagger b + \hbar\Omega_{AB}(b^\dagger a + a^\dagger b) + \varepsilon_{TLS}\sigma^z \quad (22)$$

$$-i\hbar g_A(\sigma_A^+ a + \sigma_A^- a^\dagger) - i\hbar g_B(\sigma_B^+ b + \sigma_B^- b^\dagger), \quad (23)$$

and assuming $g_A = g_B = g$, we obtain

$$S_{43} = S_{21} = 1 - \kappa_A \frac{-i(\omega - \omega'_r) + \kappa_r + \gamma_r}{-(\omega - \omega'_r)^2 + (\kappa_r + \gamma_r)^2 + \Omega_{AB}^2 - 2i(\kappa_r + \gamma_r)(\omega - \omega'_r)}. \quad (24)$$

3. Coherent drive in the Hamiltonian (Treatment of the many-photon case)

We consider the case of an incoming coherent radiation from the left-hand side of transmission line, port 1 or 3. The presence of such coherent drive is accounted for by an effective Hamiltonian

$$H = H_{sys} + H_d, \quad (25)$$

where the drive appears as a term $H_d = i\hbar J a^\dagger + H.c.$, and $J = \sqrt{\Gamma_{ext}^a} A(t)$, and $\Gamma_{ext}^a = \kappa_A$. This form is derived by assuming $\langle a_{1,in}(t) \rangle = A(t)$ and $\langle a_{2,in}(t) \rangle = \langle b_{3,in}(t) \rangle = \langle b_{4,in}(t) \rangle = 0$. The interaction of a single TLS with the resonators can be described by the Jaynes-Cummings Hamiltonian in a frame rotating at the pump frequency ω_p :

$$H = \hbar(\omega_p - \omega_A)a^\dagger a + \hbar(\omega_p - \omega_B)b^\dagger b + \frac{\hbar(\omega_p - \omega_{TLS})}{2}\sigma_z + \hbar\Omega_{AB}(b^\dagger a + a^\dagger b) - i\hbar g(\sigma^-(a^\dagger + b^\dagger) - \sigma^+(a + b)) + i\hbar J(a^\dagger - a) \quad (26)$$

The corresponding dissipation can be described by the Lindblad master equation [52]:

$$\begin{aligned}\frac{d\rho}{dt} = & -i\hbar[H_{sys}, \rho] + \Gamma_{\downarrow\uparrow}(n_{th} + 1)\mathcal{D}_\sigma(\rho) + \frac{\Gamma_\phi}{2}\mathcal{D}_{\sigma z}(\rho) \\ & + \Gamma_{\downarrow\uparrow}n_{th}\mathcal{D}_{\sigma^\dagger}(\rho) + \Gamma_{ext}^a\mathcal{D}_a(\rho) + \Gamma_{ext}^b\mathcal{D}_b(\rho),\end{aligned}\quad (27)$$

where the occupation number of TLS is $n_{th} = 1/(e^{\hbar\omega/kT} - 1)$, the damping of resonator A and B in the absence of TLS is $\Gamma_{ext}^a = \kappa_A$ and $\Gamma_{ext}^b = \kappa_B$, the TLS dephasing rate is Γ_ϕ , its rate at zero temperature $\Gamma_{\downarrow\uparrow}$, and $\mathcal{D}_A(\rho) = A\rho A^\dagger - \frac{1}{2}(A^\dagger A\rho + \rho A^\dagger A)$. Using $\langle A \rangle = \text{Tr} \langle A \rho \rangle$ and $(d/dt) \langle A \rangle = \text{Tr} \langle A(d/dt)\rho \rangle$, we can compute the Maxwell-Bloch equations

$$\frac{d\langle a \rangle}{dt} = (-i(\omega_p - \omega_a) - \frac{\Gamma_{ext}^a}{2})\langle a \rangle + g_a \langle \sigma \rangle + J \quad (28)$$

$$\frac{d\langle b \rangle}{dt} = (-i(\omega_p - \omega_b) - \frac{\Gamma_{ext}^b}{2})\langle b \rangle + g_b \langle \sigma \rangle \quad (29)$$

$$\frac{d\langle \sigma \rangle}{dt} = (-i(\omega_p - \omega_{TLS}) - \Gamma_2)\langle \sigma \rangle + g_a \langle a \sigma_z \rangle + g_b \langle b \sigma_z \rangle \quad (30)$$

$$\frac{d\langle \sigma_z \rangle}{dt} = -2g_a(\langle a^\dagger \sigma \rangle + \langle a \sigma^\dagger \rangle) - 2g_b(\langle b^\dagger \sigma^- \rangle + \langle b \sigma^+ \rangle) - \Gamma_1(\langle \sigma_z \rangle - \langle \sigma_z \rangle_{th}), \quad (31)$$

where we define $\Gamma_2 = (\Gamma_{\downarrow\uparrow}/2)(1 + 2n_{th}) + \Gamma_\phi$, $\Gamma_1 = \Gamma_{\downarrow\uparrow}(1 + 2n_{th})$, $\langle \sigma_z \rangle_{th} = -1/(1 + 2n_{th}) = -\tanh(\hbar\omega/2k_B T)$. To transform this system Eqs. (28)-(31) into a closed set of equations, we neglect the correlations and factorize the products $\langle a \sigma_z \rangle = \langle a \rangle \langle \sigma_z \rangle$, $\langle a^\dagger \sigma_z \rangle = \langle a^\dagger \rangle \langle \sigma_z \rangle$, $\langle b \sigma_z \rangle = \langle b \rangle \langle \sigma_z \rangle$, $\langle b^\dagger \sigma_z \rangle = \langle b^\dagger \rangle \langle \sigma_z \rangle$. We first determine the solution for the cavity field, $\langle a \rangle$ and $\langle b \rangle$, using the approximation $\langle a \rangle = \alpha + \delta\alpha(t)e^{-i(\omega_p - \omega_a)t}$, $\langle b \rangle = \beta + \delta\beta(t)e^{-i(\omega_p - \omega_b)t}$, $\langle \sigma \rangle = \sigma_0 + \delta\sigma(t)e^{-i(\omega_p - \omega_{TLS})t}$ and $\langle \sigma_z \rangle = \sigma_{z0}$, where $\delta\alpha(t)$, $\delta\beta(t)$ and $\delta\sigma(t)$ are slowly varying complex functions [52]. The equation for the stationary components are:

$$0 = (-i(\omega_p - \omega_a) - \frac{\Gamma_{ext}^a}{2})\alpha + g_a\sigma_0 - i\Omega_{AB}\beta + J \quad (32)$$

$$0 = (-i(\omega_p - \omega_b) - \frac{\Gamma_{ext}^b}{2})\beta + g_b\sigma_0 - i\Omega_{AB}\alpha \quad (33)$$

$$0 = (-i(\omega_p - \omega_{TLS}) - \Gamma_2)\sigma_0 + g_a\alpha\sigma_{z0} + g_b\beta\sigma_{z0} \quad (34)$$

$$0 = -2g_a(\alpha^*\sigma_0 + \alpha\sigma_0^*) - 2g_b(\beta^*\sigma_0 + \beta\sigma_0^*) - \Gamma_1(\sigma_{z0} - \langle \sigma_z \rangle_{th}). \quad (35)$$

Grouping terms by terms related to α and β , one finds

$$\sigma_0 = \frac{g_a\alpha\sigma_{z0} + g_b\beta\sigma_{z0}}{i(\omega_p - \omega_{TLS}) + \Gamma_2}. \quad (36)$$

The solution for the outfield is obtained from the boundary conditions $a_{1,(2),out} = \sqrt{\Gamma_{ext}^a}a - a_{2,(1),in}$ with inserting the assumed form of the input field $\langle a_{1,in}(t) \rangle = A(t)$. From Eq. (33) and replacing σ_0 from (36) we have

$$0 = (-i(\omega_p - \omega_b) - \frac{\Gamma_{ext}^b}{2})\beta + \frac{g_b g_a \alpha \sigma_{z0} + g_b g_b \beta \sigma_{z0}}{i(\omega_p - \omega_{TLS}) + \Gamma_2} - i\Omega_{AB}\alpha \quad (37)$$

$$0 = (-i(\omega_p - \omega_b) - \frac{\Gamma_{ext}^b}{2} + \frac{g_b g_b \sigma_{z0}}{i(\omega_p - \omega_{TLS}) + \Gamma_2})\beta + \frac{g_b g_a \alpha \sigma_{z0}}{i(\omega_p - \omega_{TLS}) + \Gamma_2} - i\Omega_{AB}\alpha \quad (38)$$

$$-(-i(\omega_p - \omega_b) - \frac{\Gamma_{ext}^b}{2} + \frac{g_b g_b \sigma_{z0}}{i(\omega_p - \omega_{TLS}) + \Gamma_2})\beta = \frac{g_b g_a \alpha \sigma_{z0}}{i(\omega_p - \omega_{TLS}) + \Gamma_2} - i\Omega_{AB} \alpha \quad (39)$$

$$-(-i(\omega_p - \omega_b) - \frac{\Gamma_{ext}^b}{2} + \frac{g_b g_b \sigma_{z0}}{i(\omega_p - \omega_{TLS}) + \Gamma_2})\beta = (\frac{g_b g_a \sigma_{z0}}{i(\omega_p - \omega_{TLS}) + \Gamma_2} - i\Omega_{AB})\alpha. \quad (40)$$

Finally we obtain

$$\beta = \frac{-\frac{g_b g_a \sigma_{z0}}{i(\omega_p - \omega_{TLS}) + \Gamma_2} + i\Omega_{AB}}{(-i(\omega_p - \omega_b) - \frac{\Gamma_{ext}^b}{2} + \frac{g_b g_b \sigma_{z0}}{i(\omega_p - \omega_{TLS}) + \Gamma_2})} \alpha \quad (41)$$

To proceed to the output fields, we next substitute the solution for β from Eq. (41) into Eq. (32)

$$0 = (-i(\omega_p - \omega_a) - \frac{\Gamma_{ext}^a}{2} + \frac{g_a g_a \sigma_{z0}}{i(\omega_p - \omega_{TLS}) + \Gamma_2})\alpha + (-i\Omega_{AB} + \frac{g_a g_b \sigma_{z0}}{i(\omega_p - \omega_{TLS}) + \Gamma_2})\beta + J \quad (42)$$

$$(i(\omega_p - \omega_a) + \frac{\Gamma_{ext}^a}{2} - \frac{g_a g_a \sigma_{z0}}{i(\omega_p - \omega_{TLS}) + \Gamma_2})\alpha + (i\Omega_{AB} - \frac{g_a g_b \sigma_{z0}}{i(\omega_p - \omega_{TLS}) + \Gamma_2})\beta = J \quad (43)$$

$$(i(\omega_p - \omega_a) + \frac{\Gamma_{ext}^a}{2} - \frac{g_a g_a \sigma_{z0}}{i(\omega_p - \omega_{TLS}) + \Gamma_2})\alpha + (i\Omega_{AB} - \frac{g_a g_b \sigma_{z0}}{i(\omega_p - \omega_{TLS}) + \Gamma_2}) \frac{-\frac{g_b g_a \sigma_{z0}}{i(\omega_p - \omega_{TLS}) + \Gamma_2} + i\Omega_{AB}}{(-i(\omega_p - \omega_b) - \frac{\Gamma_{ext}^b}{2} + \frac{g_b g_b \sigma_{z0}}{i(\omega_p - \omega_{TLS}) + \Gamma_2})} \alpha + J \quad (44)$$

$$[(i(\omega_p - \omega_a) + \frac{\Gamma_{ext}^a}{2} - \frac{g_a g_a \sigma_{z0}}{i(\omega_p - \omega_{TLS}) + \Gamma_2}) + \frac{(i\Omega_{AB} - \frac{g_a g_b \sigma_{z0}}{i(\omega_p - \omega_{TLS}) + \Gamma_2})(i\Omega_{AB} - \frac{g_a g_b \sigma_{z0}}{i(\omega_p - \omega_{TLS}) + \Gamma_2})}{(-i(\omega_p - \omega_b) - \frac{\Gamma_{ext}^b}{2} + \frac{g_b g_b \sigma_{z0}}{i(\omega_p - \omega_{TLS}) + \Gamma_2})}] \alpha = \sqrt{\Gamma_{ext}^a} a_{1,in}. \quad (45)$$

The solution for the resonator α field is

$$\alpha = \frac{\sqrt{\Gamma_{ext}^a}}{[(i(\omega_p - \omega_a) + \frac{\Gamma_{ext}^a}{2} - \frac{g_a g_a \sigma_{z0}}{i(\omega_p - \omega_{TLS}) + \Gamma_2}) + \frac{(i\Omega_{AB} - \frac{g_a g_b \sigma_{z0}}{i(\omega_p - \omega_{TLS}) + \Gamma_2})^2}{(-i(\omega_p - \omega_b) - \frac{\Gamma_{ext}^b}{2} + \frac{g_b g_b \sigma_{z0}}{i(\omega_p - \omega_{TLS}) + \Gamma_2})}]} a_{1,in}. \quad (46)$$

Using this result one can find transmission and reflection coefficient using the boundary condition $a_{2,out} = \sqrt{\Gamma_{ext}^a} a - a_{1,in}$. The transmission, $S_{21} = \frac{a_{2,out}}{a_{1,in}}$ can be written as

$$S_{21} = 1 - \frac{\Gamma_{ext}^a}{[(i(\omega_p - \omega_a) + \frac{\Gamma_{ext}^a}{2} - \frac{g_a g_a \sigma_{z0}}{i(\omega_p - \omega_{TLS}) + \Gamma_2}) + \frac{(i\Omega_{AB} - \frac{g_a g_b \sigma_{z0}}{i(\omega_p - \omega_{TLS}) + \Gamma_2})^2}{(-i(\omega_p - \omega_b) - \frac{\Gamma_{ext}^b}{2} + \frac{g_b g_b \sigma_{z0}}{i(\omega_p - \omega_{TLS}) + \Gamma_2})}]}}, \quad (47)$$

where

$$\sigma_{z0} = \langle \sigma_z \rangle_{th} [1 - \frac{\Gamma_2^2 \bar{n}/n_s}{(\omega_{TLS} - \omega_p) + \Gamma_2^2 (1 + \bar{n}/n_s)}], \quad (48)$$

and $\bar{n} = |A(t)|^2$ is the mean photon number in the cavity and $n_s^{-1} = 4g^2/\Gamma_1 \Gamma_2$ the number of photons required to saturate the TLS transition.

3. Correlation amplitude:

TLS frequency (1/f) noise gives noise in resonator transmission (e.g. S_{21}), where the transmission changes in phase and amplitude generally for one input frequency. The noise is mainly seen in a particular direction in IQ space as fluctuations in $[\text{Re}(S_{21}(f_{0A})), \text{Im}(S_{21}(f_{0A}))]$ and $[\text{Re}(S_{21}(f_{0B})), \text{Im}(S_{21}(f_{0B}))]$ which are tangent to the complex transmission plot, which we use (Eq. (18)) to define the quadratures $[Q'_A, I'_A]$ and $[Q'_B, I'_B]$ shown in Fig. 5(c). As in a standard KID, the fluctuation quadrature is thus frequency noise. However, now we have two input frequencies

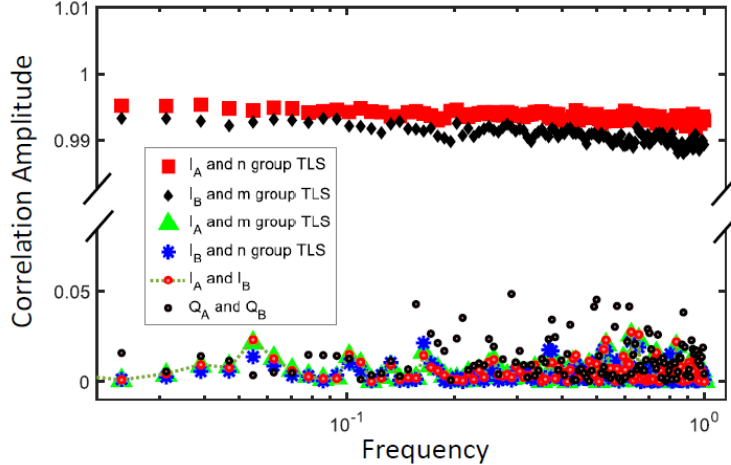


FIG. 9. Correlation amplitude C_{xy} between noise quantities: 1/f-noise TLS frequencies and resonator transmission quadratures (I_A , Q_A , I_B and Q_B). 1/f noise sources from m-group TLS and n group TLS are not correlated as there is no significant TLS-TLS coupling mechanism. There is near perfect noise correlation between I_A and n-group TLS, and I_B and m-group TLS. There is no significant normalized correlation between resonator quadratures I_A and I_B because the noise fluctuations occur as a m- or n- group TLS source on a corresponding resonator quadrature I_A or I_B . This implies that noise is not significantly correlated through the resonator-resonator coupling. Q_A and Q_B have slightly larger normalized correlation amplitude, but also this is of no consequence because these quadratures have small noise powers.

and two TLS noise sources. The TLSs induce noise in the resonators, where I'_A and I'_B in Fig. 5(c) are defined to be tangent to the transmission versus frequency plot near the probe frequencies [f_A , f_B]. In Fig. 9 we show the correlation amplitude (the normalized cross spectral density)

$$C_{xy} = \frac{S_{\nu}^{xy}}{(S_{\nu}^{xx} S_{\nu}^{yy})^{1/2}}, \quad (49)$$

between different quadratures and TLS groups. Here, x and y are the different possible aforementioned TLS and quadrature noise types. S_{ν}^{xy} is the cross-spectral density between x and y, and S_{ν}^{xx} and S_{ν}^{yy} are the autospectral density of x and y respectively. The result plotted in Fig. 9 shows that the 1/f noise on each mode and its own TLS fluctuations are highly correlated, but the noise induced on the measurement quadratures of the two resonator modes is uncorrelated.

* Correspondence and requests for materials should be addressed to NF (email: nforouzani@lps.umd.edu) or KDO (email: osborn@lps.umd.edu).

- [1] P. K. Day, H. G. LeDuc, B. A. Mazin, A. Vayonakis, and J. Zmuidzinas, A broadband superconducting detector suitable for use in large arrays, *Nature* 425, no. 6960, 817–821, (2003).
- [2] B. A. Mazin, Ph.D. thesis, Microwave kinetic inductance detectors, Caltech, (2004).
- [3] J. Gao, J. Zmuidzinas, B. A. Mazin, H. G. LeDuc, and P. K. Day, Noise properties of superconducting coplanar waveguide microwave resonators, *Appl. Phys. Lett.* 90, 102507 (2007).
- [4] Omid Norooziana, Jiansong Gaob, Jonas Zmuidzinas, Henry G. LeDucc, and Benjamin A. Mazind, Two-level system noise reduction for Microwave Kinetic Inductance Detectors, *Conference Proceedings* 1185, 148 (2009).
- [5] Steffen Schlör, Jürgen Lisenfeld, Clemens Müller, Alexander Bilmes, Andre Schneider, David P. Pappas, Alexey V. Ustinov, and Martin Weides, Correlating decoherence in transmon qubits: low frequency noise by single fluctuators, *Phys. Rev. Lett.* 123, 190502 (2019).
- [6] Oliver Dial et al., Bulk and surface loss in superconducting transmon qubits, *Supercond. Sci. Technol.* 29 044001 (2016).
- [7] J. Burnett et al., Evidence for interacting two-level systems from the 1/f noise of a superconducting resonator. *Nat Commun* 5, 4119 (2014). <https://doi.org/10.1038/ncomms5119>
- [8] J. Gao, M. Daal, A. Vayonakis, S. Kumar, J. Zmuidzinas, B. Sadoulet, B. A. Mazin, P. K. Day, and H. G. Leduc, Experimental evidence for a surface distribution of two-level systems in superconducting lithographed microwave resonators, *Appl. Phys. Lett.* 92, 152505 (2008), <https://doi.org/10.1063/1.2906373>
- [9] C.R.H. McRae, H. Wang, J. Gao, M. R. Vissers, T. Brecht, A. Dunsworth, D. P. Pappas, and J. Mutus, Materi-

als loss measurements using superconducting microwave resonators, *Review of Scientific Instruments* 91, 091101 (2020) <https://doi.org/10.1063/5.0017378>

[10] P. R. Maloney, N. G. Czakon, P. K. Day, T. P. Downes, R. Duan and J. Gao, J. Glenn, S. R. Golwala, M. I. Hollister, H. G. LeDuc, B. A. Mazin, S. G. McHugh, O. Noroozian, H. T. Nguyen, J. Sayers, J. A. Schlaerth, S. Siegel, J. E. Vaillancourt, A. Vayonakis, P. Wilson and J. Zmuidzinas, Millimeter, submillimeter, and far-infrared detectors and instrumentation for astronomy V, *MUSIC for sub/millimeter astrophysics*, SPIE publisher, 124-134, (2010).

[11] A. Monfardini et al., A dual-band millimeter-wave kinetic inductance camera for the IRAM 30 m telescope, *2011 ApJS* 194 24 (2011).

[12] N. Galitzki et al., Millimeter, submillimeter, and far-infrared detectors and instrumentation for astronomy VII, *International Society for Optics and Photonics*, 108-118, (2016).

[13] E. L. Wright, G. Hinshaw, C. L. Bennett, Producing Megapixel Cosmic Microwave Background from Differential Radiometer Data, *Astrophysical Journal Letters* v.458, p.L53 (1996).

[14] D. Maino, C. Burigana, K. M. Górski, N. Mandolesi, M. Bersanelli, Removing 1/f noise stripes in cosmic microwave background anisotropy observations, *Astronomy and Astrophysics*, v.387, p.356-365 (2002).

[15] N. J. Miller et al., Recovery of large angular scale CMB polarization for instruments employing variable-delay polarization modulators, *ApJ* 818 151 (2016).

[16] Steven Hailey-Dunsheath, Reinier M. J. Janssen, Jason Glenn, Charles M. Bradford, Joanna Perido, Joseph Redford, Jonas Zmuidzinas, Kinetic inductance detectors for the Origins Space Telescope, *J. of Astronomical Telescopes, Instruments, and Systems*, 7(1), 011015 (2021).

[17] Johnson, B.R., Flanigan, D., Abitbol, M.H. et al. Development of multi-chroic MKIDs for next-generation CMB polarization studies. *J Low Temp Phys* 193, 103–112 (2018).

[18] J. van Rantwijk, M. Grim, D. van Loon, S. Yates, A. Baryshev and J. Baselmans, "Multiplexed readout for 1000-pixel arrays of microwave kinetic inductance detectors," in *IEEE Transactions on Microwave Theory and Techniques*, vol. 64, no. 6, pp. 1876-1883, June 2016, doi: 10.1109/TMTT.2016.2544303.

[19] Clemens Müller, Jürgen Lisenfeld, Alexander Shnirman, and Stefano Poletto, Interacting two-level defects as sources of fluctuating high-frequency noise in superconducting circuits, *Phys Rev B* 92, 035442 (2015).

[20] J. Kelly, R. Barends, A. G. Fowler, A. Megrant, E. Jeffrey, T. C. White, D. Sank, J. Y. Mutus, B. Campbell, Yu Chen, Z. Chen, B. Chiaro, A. Dunsworth, E. Lucero, M. Neeley, C. Neill, P. J. J. O’Malley, C. Quintana, P. Roushan, A. Vainsencher, J. Wenner, and John M. Martinis, Scalable in situ qubit calibration during repetitive error detection, *Phys Rev A* 94, 032321 (2016)

[21] John M. Martinis, K. B. Cooper, R. McDermott, Matthias Steffen, Markus Ansmann, K. D. Osborn, K. Cicak, Seongshik Oh, D. P. Pappas, R. W. Simmonds, and Clare C. Yu, Decoherence in Josephson Qubits from Dielectric Loss, *PRL* 95, 210503 (2005)

[22] Jiansong Gao and Jonas Zmuidzinas, Noise properties of superconducting coplanar waveguide microwave resonators, *App Phys Lett* 90, 102507 (2007)

[23] Jiansong Gao, Miguel Daal, John M. Martinis, Anastasios Vayonakis, Jonas Zmuidzinas, Bernard Sadoulet, Benjamin A. Mazin, Peter K. Day, and Henry G. Leduc, A semiempirical model for two-level system noise in superconducting microresonators, *Appl Phys Lett* 92 212504 (2008)

[24] Lara Faoro and Lev B. Ioffe, Interacting tunneling model for two-level systems in amorphous materials and its predictions for their dephasing and noise in superconducting microresonators, *Phys Rev B* 91, 014201 (2015)

[25] M Schechter et al., Nonuniversality and strongly interacting two-level systems in glasses at low temperatures, *New J. Phys.* 20 063048 (2018).

[26] Yoni Shalibo, Ya’ara Rofe, David Shwa, Felix Zeides, Matthew Neeley, John M. Martinis, and Nadav Katz, Lifetime and Coherence of Two-Level Defects in a Josephson Junction, *Phys. Rev. Lett.* 105, 177001(2010).

[27] R. W. Simmonds, K. M. Lang, D. A. Hite, S. Nam, D. P. Pappas, and John M. Martinis, Decoherence in Josephson Phase Qubits from Junction Resonators, *Phys. Rev. Lett.* 93, 077003 (2004)

[28] M. Steffen, M. Sandberg, S. Srinivasan, Recent research trends for high coherence quantum circuits, *Supercond. Sci. Technol.* 30, 030301 (2017).

[29] Chu, Y. et al. Suspending superconducting qubits by silicon micromachining. *Phys. Lett.* 109, 112601 (2016).

[30] Burnett, J. et al. Evidence for interacting two-level systems from the 1/f noise of a superconducting resonator. *Nat. Commun.* 5, 4119 (2014).

[31] Neill, C. et al. Fluctuations from edge defects in superconducting resonators. *Appl. Phys. Lett.* 103, 072601 (2013).

[32] Stephen J. C. Yates, Juan Bueno, Akira Endo, Andrey M. Baryshev, Lorenza Ferrari, Vignesh Murugesan, David J. Thoen, Jochem J. A. Baselmans, On the design and performance of very large MKID arrays, *Proceedings Volume* 11453, *Millimeter, Submillimeter, and Far-Infrared Detectors and Instrumentation for Astronomy X*; 114530C (2020).

[33] De Visser, P.J., Quasiparticle dynamics in aluminium superconducting microwave resonators, *Delft University of Technology* (2014).

[34] Benjamin A. Mazin, Kieran O’Brien, Sean McHugh, Bruce Bumble, David Moore, Sunil Golwala, Jonas Zmuidzinas, ARCHONS: a highly multiplexed superconducting optical to near-IR camera, *Proceedings Volume* 7735, *Ground-based and Airborne Instrumentation for Astronomy III*; 773518 (2010) <https://doi.org/10.1117/12.856440>

[35] Hanhee Paik (and Kevin D. Osborn, Reducing quantum-regime dielectric loss of silicon nitride for superconducting quantum circuits, *Appl. Phys. Lett.* 96, 072505 (2010).

[36] M. R. Vissers, J. Hubmayr, M. Sandberg, S. Chaudhuri, C. Bockstiegel, and J. Gao, Frequency-tunable superconducting resonators via nonlinear kinetic inductance, *Appl. Phys. Lett.* 107, 062601 (2015).

[37]

[38] S. J. Weber, K. W. Murch, D. H. Slichter, R. Vijay, and I. Siddiqi, Single crystal silicon capacitors with low microwave loss in the single photon regime, *Appl. Phys. Lett.* 98, 172510 (2011).

[39] Cataldo, G., Wollack, E.J., et al., Analysis and Calibration Techniques for Superconducting Resonators, *Review of Scientific Instruments*, Vol. 86:1 ; Iss. 1, 013103 (2015).

[40] C. W. Gardiner and M. J. Collett, Input and output in damped quantum systems: Quantum stochastic differential equations and the master equation, *Phys. Rev. A* 31, 3761 (1985).

[41] D. F. Walls and G. Milburn, *Quantum Optics* (Springer, Berlin, 2008).

[42] M. Tavis and F. W. Cummings, *Phys. Rev.* 170, 379 (1968), .

[43] J. M. Fink, M. Göppl, M. Baur, R. Bianchetti, P. J. Leek, A. Blais, and A. Wallraff, Climbing the Jaynes-Cummings ladder and observing its nonlinearity in a cavity QED system, *Nature* 454, 315-318 (2008).

[44] J. M. Fink, R. Bianchetti, M. Baur, M. Göppl, L. Steffen, S. Filipp, P. J. Leek, A. Blais, and A. Wallraff, Dressed collective qubit states and the Tavis-cummings model in circuit QED, *Phys. Rev. Lett.* 103, 083601 (2009).

[45] B. Sarabi, A. N. Ramanayaka, A. L. Burin, F. C. Wellstood, and K. D. Osborn, Cavity quantum electrodynamics using a near-resonance two-level system: Emergence of the Glauber state, *Appl. Phys. Lett.* 106, 172601 (2015).

[46] Juha Leppäkangas, Jan David Brehm, Ping Yang, Lingzhen Guo, Michael Marthaler, Alexey V. Ustinov, and Martin Weides, Resonance inversion in a superconducting cavity coupled to artificial atoms and a microwave background, *Phys. Rev. A* 99, 063804 (2019).

[47] T. R. Stevenson, Limits on the sensitivity of spherical gravitational wave detectors and on the accuracy of reconstructed signals, *Phys. Rev. D* 56, 564 (1997).

[48] M. S. Khalil, M. J. A. Stoutimore, F. C. Wellstood, and K. D. Osborn, An analysis method for asymmetric resonator transmission applied to superconducting devices, *Journal of Applied Physics* 111, 054510 (2012).

[49] B. Sarabi, Cavity quantum electrodynamics of nanoscale two-level systems, University of Maryland, (2014).

[50] S. Hunklinger and A. K. Raychaudhuri, Thermal and elastic anomalies in glasses at low temperatures. *Prog. Low Temp. Phys.*, 9:267 344, (1986).

[51] J. Classen, C. Enss, C. Bechinger, G. Weiss, and S. Hunklinger, Low frequency acoustic and dielectric measurements on glasses. *Annalen der Physik*, 506(5):315335, (1994).

[52] T. Capelle et al., Probing a two-level system bath via the frequency shift of an off-resonantly driven cavity, *Phys. Rev. Applied* 13, 034022 (2020).